

Multi-fidelity Aerodynamic Shape Optimization Using Manifold Mapping

Jie Ren¹ and Leifur Leifsson²
Iowa State University, Ames, Iowa, 50011

Slawomir Koziel³ and Yonatan Tesfahunegn⁴
Engineering Optimization & Modeling Center, Reykjavik University, Menntavegur 1, 101 Reykjavik, Iceland

A computationally efficient optimization algorithm for aerodynamic design is presented. In our approach, direct optimization of a computationally expensive model is replaced by an iterative updating and re-optimization of a fast physics-based replacement model, following the surrogate-based optimization paradigm. The surrogate is constructed using a low-fidelity model which is corrected using manifold mapping (MM) to become a reliable representation of the high-fidelity one during the optimization process. MM exploits the high-fidelity simulation data accumulated in the course of the optimization run gradually improving the generalization capability of the surrogate. The version of MM utilized here does not require gradient information. The method is applied to lift-constrained airfoil drag minimization in two-dimensional inviscid and viscous transonic flows. MM yielded optimized shapes, with 8 B-spline design variables, that are comparable to the shapes obtained by direct optimization algorithms equipped with adjoint sensitivities and trust regions. In the inviscid benchmark case, MM needed less than 150 equivalent high-fidelity model evaluations (only flow solutions), or approximately 460 minutes on a HPC with 32 processors, whereas the direct algorithm needed 391 high-fidelity model evaluations (flow and adjoint), or approximately 4,494 minutes on the same HPC. For the viscous case, MM yields an optimized shape using less than 125 equivalent high-fidelity evaluations, taking approximately 17.4 hours on the HPC. The direct algorithm was unsuccessful in optimizing the baseline shape in this case.

I. Introduction

Computationally robust and fast optimization algorithms are essential in the design of engineering systems.^{1,2} This is particularly the case when accurate and CPU-intensive high-fidelity simulations are needed to analyze systems with nonlinear physics and multidisciplinary couplings. The combination of a high computational cost of the simulations and a multi-dimensional design space, i.e., consisting of more than 10 design variables, constitutes a design problem which can be impractical to solve with conventional optimization techniques,³⁻⁹ even when using high-performance computing clusters.

Cost-effective design can be performed using surrogate-based optimization (SBO) techniques.¹⁰⁻¹³ In SBO, the direct optimization of the high-fidelity model is replaced by an iterative correction-prediction process where a surrogate model (a computationally cheap representation of the high-fidelity one) is constructed and subsequently exploited to obtain an approximate location of the high-fidelity model optimal design.

In general, the SBO approaches differ in how the surrogate model is constructed and updated. Data-driven surrogates are constructed by approximating sampled high-fidelity model data using techniques such as polynomial approximation, radial basis functions, kriging, neural networks, or support vector regression (see, for example, Queipo *et al.*¹⁰, and Forrester and Keane¹¹). Numerous methods for allocating additional training points (the so-called infill criteria) for the sake of enhancing the surrogate have been developed, aiming either at global modeling accuracy or locating globally optimal design (or a trade-offs between the two)¹¹. Physics-based surrogates, also

¹ Graduate Student, Department of Aerospace Engineering, Student Member AIAA.

² Assistant Professor, Department of Aerospace Engineering, Senior Member AIAA.

³ Professor, School of Science and Engineering, Senior Member AIAA.

⁴ Post-doctoral Fellow, School of Science and Engineering, Member AIAA.

referred to as multi-fidelity ones, are constructed by correcting/enhancing physics-based low-fidelity models.¹²⁻¹⁴ A low-fidelity model, or a simplified description of the system under consideration, can be obtained by neglecting certain physical or second-order effects, using simplified equations, or by exploiting the high-fidelity model with a coarser computational description.¹³ The low-fidelity models are subsequently corrected or enhanced to become a reliable representation of the high-fidelity model by specific methods such as multiplicative or additive corrections¹², space mapping^{15,16} (SM), adaptive response correction¹⁷ (ARC), adaptive response prediction¹⁸ (ARP), or shape-preserving response prediction¹⁹ (SPRP).

Data-driven surrogates can be the basis of efficient global optimization techniques¹¹. However, to ensure decent accuracy, approximation surrogates require a large number of data samples. Moreover, the number of samples grows exponentially with the problem dimensionality. Although the physical surrogate models are not as versatile as the approximation-based ones, they have the potential to offer significantly better efficiency in terms of the computational cost¹²⁻¹⁴. Many algorithms require only a single high-fidelity model evaluation per design iteration¹². Consequently, physic-based surrogates may exhibit better generalization capability than the approximation ones.

In this work, we focus on optimization using multi-fidelity models. Perhaps the simplest way of constructing the physics-based surrogate is through a response correction. Various correction techniques and related optimization algorithms have been developed over the years, including approximation and model management optimization¹³ (AMMO) involving first- and higher-order correction terms, multi-point correction techniques^{15,16}, several variations of output space mapping¹⁵, as well as manifold mapping^{20,21}. Apart from the aforementioned ones, which are all so-called parametric methods¹² (where the correction functions are given explicitly with the parameters usually obtained by explicit calculations or solving auxiliary linear regression problems), a number of non-parametric technique have been developed, already mentioned above (SPRP, ARC, ARP). Parametric methods are preferred by many due to their simplicity. Among these, manifold mapping^{20,21} (MM) seems to be one of the most interesting because is its capability to accommodate available high-fidelity model data accumulated during the optimization run, as well as having the potential to approximately satisfy the first-order consistency with the high-fidelity model upon the algorithm convergence.

Despite its potential, manifold mapping^{20,21} has not yet been applied to aerodynamic shape optimization (ASO). In this paper, we utilize MM for constructing surrogate models in multi-fidelity ASO. We use multi-fidelity aerodynamics models based on computational fluid dynamics simulations for two-dimensional transonic flows. The theory of the approach and the challenges related to the application of manifold mapping in conjunction with physics-based low-fidelity models are described when applied to challenging design problems. Furthermore, we discuss the possibility of combining MM with multi-point space mapping^{15,16} (SM), where a quasi-global SM correction is utilized for low-fidelity model preconditioning for the purpose of improving the MM algorithm performance.

The paper is organized in the following way. We begin by giving the details of the optimization methodology, including several approaches for solving the ASO problem using direct and multi-fidelity search algorithms. The performance of the search algorithms are compared when applied to benchmark aerodynamic design problems involving two-dimensional inviscid and viscous transonic flow past airfoils. The paper ends with conclusions.

II. Aerodynamic Shape Optimization

This section describes the algorithmic approach proposed for solving the ASO problems in a computationally efficient manner. First, the ASO problem formulation is given. Then, the details of two direct optimization algorithms (for benchmarking purposes) are provided. These algorithms will be used for benchmarking purposes. The section ends with a description of multi-fidelity optimization using space mapping (also for benchmarking purposes), and the proposed algorithm.

A. Problem Formulation

The aerodynamic design problems considered in this work involve lift-constrained drag minimization of airfoils in two-dimensional transonic flow. The flow simulations are performed using accurate, but computationally expensive, high-fidelity computational fluid dynamics (CFD) models. These models are denoted here by \mathbf{f} . In general, nonlinear constrained optimization problems can be formulated as

$$\mathbf{x}^* = \arg \min_{\mathbf{x}} H(\mathbf{f}(\mathbf{x})) \text{ s.t. } \mathbf{g}(\mathbf{x}) \leq 0, \mathbf{h}(\mathbf{x}) = 0, \mathbf{l} \leq \mathbf{x} \leq \mathbf{u}, \quad (1)$$

where \mathbf{x} is the design variable vector of size $p \times 1$, \mathbf{x}^* is the optimized design, H is a scalar valued objective function, $\mathbf{f}(\mathbf{x})$ is a vector of size $q \times 1$ with the figures of merit, $\mathbf{g}(\mathbf{x})$ is a vector of size $M \times 1$ with the inequality constraints, $\mathbf{h}(\mathbf{x})$ is a vector of size $N \times 1$ with the equality constraints, and \mathbf{l} and \mathbf{u} are the design variable lower and upper bounds, respectively, both vectors of the same size as \mathbf{x} . The vectors $\mathbf{f}(\mathbf{x})$, $\mathbf{g}(\mathbf{x})$, and $\mathbf{h}(\mathbf{x})$ are all obtained, or derived, from computationally expensive models.

In ASO, the high-fidelity model \mathbf{f} calculates the figures of merit, e.g., in the two-dimensional case \mathbf{f} can be composed as follows: $\mathbf{f}(\mathbf{x}) = [C_{l,f}(\mathbf{x}) \ C_{d,f}(\mathbf{x}) \ A(\mathbf{x})]^T$ where $C_{l,f}(\mathbf{x})$ is the nondimensional lift coefficient, $C_{d,f}(\mathbf{x})$ is the nondimensional drag coefficient, and $A(\mathbf{x})$ the airfoil cross-sectional area. The subscript f denotes the high-fidelity model. In the case of a drag minimization problem, the objective function in (1) is set as $H(\mathbf{f}(\mathbf{x})) = C_{d,f}(\mathbf{x})$. The inequality constraints are set as $g_1(\mathbf{x}) = C_{m,min} - C_{m,f}(\mathbf{x}) \leq 0$, and $g_2(\mathbf{x}) = A_{min} - A(\mathbf{x}) \leq 0$, where $C_{m,min}$ is a minimum allowable pitching moment coefficient, $C_{m,f}(\mathbf{x})$ is the pitching moment of the current design \mathbf{x} , A_{min} is a minimum cross-sectional area, and $A(\mathbf{x})$ the cross-sectional area of the design \mathbf{x} . The equality constraint is $h_1(\mathbf{x}) = C_{l,t} - C_{l,f}(\mathbf{x}) = 0$, where $C_{l,t}$ is the target lift coefficient, and $C_{l,f}(\mathbf{x})$ is the lift coefficient of the current design. Here, the angle of attack, α , is used as a dummy variable to find the target lift coefficient value. All the constraints are handled directly in the optimization process.

B. Direct Optimization

Direct optimization, used here for comparison and validation purposes, can be broadly categorized into derivative-free and gradient-based approaches.¹² Methods of the derivative-free type are typically more costly than their gradient-based counterparts, but have the benefit of being more immune to numerical noise. The latter may be present when using CFD simulation models, especially with coarse discretization of the structure at hand. Due to the availability of adjoint technology²², it is possible to perform direct gradient-based optimization of computationally expensive simulation models. Using this technology, the cost of obtaining the gradients is almost equivalent to one flow solution for any number of design variables.

In this work, the manifold mapping algorithm^{20,21} is compared with direct optimization of the high-fidelity model \mathbf{f} using a gradient-based algorithm exploiting adjoint sensitivities and trust regions²³. More specifically, the problem (1) is solved as an iterative process²⁴

$$\mathbf{x}^{(i+1)} = \arg \min_{\mathbf{x}, \|\mathbf{x} - \mathbf{x}^{(i)}\| \leq \delta^{(i)}} H(\mathbf{s}^{(i)}(\mathbf{x})), \quad (2)$$

where $\mathbf{x}^{(i)}$, $i = 0, 1, \dots$, is a sequence of approximate solutions to (1), whereas $\mathbf{s}_k^{(i)}(\mathbf{x})$ is a linear expansion of $\mathbf{f}(\mathbf{x})$ at $\mathbf{x}^{(i)}$ defined as

$$\mathbf{s}^{(i)}(\mathbf{x}) = \mathbf{f}(\mathbf{x}^{(i)}) + \nabla \mathbf{f}(\mathbf{x}^{(i)}) \cdot (\mathbf{x} - \mathbf{x}^{(i)}). \quad (3)$$

Here, the gradient of the model \mathbf{f} (applies separately for the drag and lift coefficient) is obtained by the adjoint equation (see, e.g., Jameson²²). The linear model (3) satisfies the zero- and first-order consistency conditions with the function $\mathbf{s}_k^{(i)}(\mathbf{x})$ at $\mathbf{x}^{(i)}$, i.e., $\mathbf{s}_k^{(i)}(\mathbf{x}^{(i)}) = \mathbf{f}(\mathbf{x}^{(i)})$, and $\nabla \mathbf{s}_k^{(i)}(\mathbf{x}^{(i)}) = \nabla \mathbf{f}(\mathbf{x}^{(i)})$. Optimization of the linear model is constrained to the vicinity of the current design defined as $\|\mathbf{x} - \mathbf{x}^{(i)}\| \leq \delta^{(i)}$, with the trust region radius $\delta^{(i)}$ adjusted adaptively using the standard trust region rules²³. The termination conditions for the algorithm (2) are: (i) $\|\mathbf{x}^{(i)} - \mathbf{x}^{(i-1)}\| < \varepsilon_x$, (ii) $|H^{(i)} - H^{(i-1)}| < \varepsilon_H$, (iii) $\delta^{(i)} < \varepsilon_\delta$, where ε_x , ε_H , and ε_δ are user defined convergence tolerances. For direct optimization of the aerodynamics design benchmark problems, we use: $\varepsilon_x = 10^{-6}$, $\varepsilon_H = 10^{-7}$, and $\varepsilon_\delta = 10^{-6}$. The solution of algorithm (2) with the model (3) is carried out using the pattern search algorithm^{24,25} and MATLAB's fmincon algorithm²⁶.

1. Pattern Search

The pattern search algorithm^{24,25} is a stencil-based local optimization method that explores the neighborhood of the current design point. A rectangular grid (i.e., one point in each direction and in each dimension) is used in our implementation. The search process utilizes grid-constrained line search with the search direction determined using the objective function gradient estimated from perturbed designs. In case of a failure the best perturbation (if better than the current design) is selected. Finally, the grid is refined in case the poll step does not lead to an improved design. The poll stage of the pattern search process is illustrated below in Fig. 1. For more information about the particular pattern search algorithm used for this study, refer to Refs. 24, and 25.

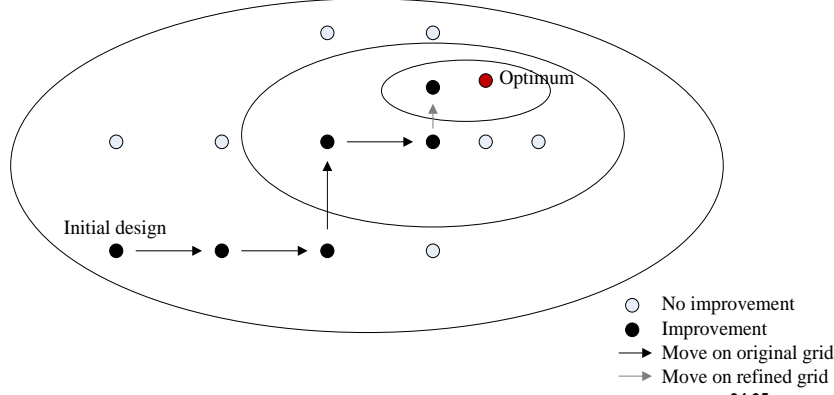


Figure 1. An illustration of the pattern search algorithm^{24,25}.

2. MATLAB's *fmincon*

Matlab's *fmincon*²⁶ utilizes several optimization algorithms (depending on the user preference as well as the scale of the problem at hand). These include trust region reflective algorithm where the objective function is represented using its linear or quadratic expansion models optimized using standard trust region rules²³, a sequential quadratic programming (SQP) algorithm, where the original problem is solved iteratively by replacing the original objective function (and nonlinear constraints) by their respective local quadratic models (linear for constraint functions), as well as an interior point algorithm, where the original constrained problem is replaced by a sequence of approximate minimization problems using a barrier method. In this work, we use the interior point algorithm.

C. Multi-fidelity Optimization

A generic multi-fidelity optimization algorithm with trust regions produces a sequence $\mathbf{x}^{(i)}$, $i = 0, 1, \dots$, of approximate solutions to (1) using (2) with a surrogate model $\mathbf{s}^{(i)}(\mathbf{x})$ iteration i .¹² The surrogate model \mathbf{s} is a suitably corrected low-fidelity model \mathbf{c} . In this work, two (parametric) correction methods are considered: space mapping¹⁶ (for the sake of comparison and validation) and manifold mapping^{20,21}.

The key component of multi-fidelity optimization algorithms is the physics-based low-fidelity (or coarse) model \mathbf{c} that embeds certain knowledge about the system under consideration, and allows us to construct a reliable surrogate using a limited amount of high-fidelity model data. Here, the low-fidelity model is evaluated using the same CFD solver as the high-fidelity model \mathbf{f} , so that both models share the same “knowledge” of the system under design. The details of each model are given for each benchmark case study given in Section III.

1. Multi-point Space Mapping

Multi-point SM constructs an aerodynamic surrogate model as follows¹⁶:

$$\mathbf{s}^{(i)}(\mathbf{x}) = \mathbf{A}^{(i)} \circ \mathbf{c}(\mathbf{x}) + \mathbf{D}^{(i)} + \mathbf{q}^{(i)} = [a_l^{(i)} C_{l,c}(\mathbf{x}) + d_l^{(i)} + q_l^{(i)} \quad a_d^{(i)} C_{d,c}(\mathbf{x}) + d_d^{(i)} + q_d^{(i)} \quad A_c(\mathbf{x})]^T, \quad (4)$$

where \circ denotes component-wise multiplication. Note that there is no need to map A_c because $A_c(\mathbf{x}) = A_f(\mathbf{x})$ for all \mathbf{x} . The response correction parameters $\mathbf{A}^{(i)}$ and $\mathbf{D}^{(i)}$ are obtained by solving

$$[\mathbf{A}^{(i)}, \mathbf{D}^{(i)}] = \arg \min_{[\mathbf{A}, \mathbf{D}]} \sum_{k=0}^i \|\mathbf{f}(\mathbf{x}^{(k)}) - \mathbf{A} \circ \mathbf{c}(\mathbf{x}^{(k)}) + \mathbf{D}\|^2, \quad (5)$$

i.e., the response scaling is supposed to (globally) improve the matching for all previous iteration points. The additive response correction term $\mathbf{q}^{(i)}$ is defined as

$$\mathbf{q}^{(i)} = \mathbf{f}(\mathbf{x}^{(i)}) - [\mathbf{A}^{(i)} \circ \mathbf{c}(\mathbf{x}^{(i)}) + \mathbf{D}^{(i)}], \quad (6)$$

i.e., it ensures perfect matching between the surrogate and the high-fidelity model at the current design $\mathbf{x}^{(i)}$, $\mathbf{s}^{(i)}(\mathbf{x}^{(i)}) = \mathbf{f}(\mathbf{x}^{(i)})$ (zero-order consistency).

The term $\mathbf{q}^{(i)}$ can be calculated using (6). $\mathbf{A}^{(i)}$ and $\mathbf{D}^{(i)}$ can be obtained analytically as¹⁶

$$\begin{bmatrix} a_l^{(i)} \\ d_l^{(i)} \end{bmatrix} = (\mathbf{C}_l^T \mathbf{C}_l)^{-1} \mathbf{C}_l^T \mathbf{F}_l, \quad \begin{bmatrix} a_d^{(i)} \\ d_d^{(i)} \end{bmatrix} = (\mathbf{C}_d^T \mathbf{C}_d)^{-1} \mathbf{C}_d^T \mathbf{F}_d, \quad (7)$$

where

$$\mathbf{C}_l = \begin{bmatrix} C_{l,c}(\mathbf{x}^{(0)}) & C_{l,c}(\mathbf{x}^{(1)}) & \cdots & C_{l,c}(\mathbf{x}^{(i)}) \\ 1 & 1 & \cdots & 1 \end{bmatrix}^T, \quad \mathbf{F}_l = [C_{l,f}(\mathbf{x}^{(0)}) \quad C_{l,f}(\mathbf{x}^{(1)}) \quad \cdots \quad C_{l,f}(\mathbf{x}^{(i)})]^T, \quad (8)$$

$$\mathbf{C}_d = \begin{bmatrix} C_{d,c}(\mathbf{x}^{(0)}) & C_{d,c}(\mathbf{x}^{(1)}) & \cdots & C_{d,c}(\mathbf{x}^{(i)}) \\ 1 & 1 & \cdots & 1 \end{bmatrix}^T, \quad \mathbf{F}_d = [C_{d,f}(\mathbf{x}^{(0)}) \quad C_{d,f}(\mathbf{x}^{(1)}) \quad \cdots \quad C_{d,f}(\mathbf{x}^{(i)})]^T, \quad (9)$$

which is a least-square optimal solution to the linear regression problem $\mathbf{C}_l a_l^{(i)} + d_l^{(i)} = \mathbf{F}_l$ and $\mathbf{C}_d a_d^{(i)} + d_d^{(i)} = \mathbf{F}_d$, equivalent to (5). Note that the matrices $\mathbf{C}_l^T \mathbf{C}_l$ and $\mathbf{C}_d^T \mathbf{C}_d$ are non-singular for $i > 1$. For $i = 1$ only the multiplicative correction with $\mathbf{A}^{(i)}$ components are used, which can be calculated in a similar way.

The solution of algorithm (2) with the surrogate model (4) is carried out using the pattern search algorithm,^{24,25} and the termination conditions are the same as for the direct optimization algorithm (Sec. II.B) but with $\varepsilon_x = 10^{-3}$, $\varepsilon_H = 10^{-4}$, and $\varepsilon_\delta = 10^{-3}$.

2. Manifold Mapping

Manifold mapping (MM) is a simple yet interesting response correction technique that is capable of comprehensive exploitation of available high-fidelity model data. In its basic version, the MM surrogate model is defined as^{20,21}

$$\mathbf{s}^{(i)}(\mathbf{x}) = \mathbf{f}(\mathbf{x}^{(i)}) + \mathbf{S}^{(i)}(\mathbf{c}(\mathbf{x}) - \mathbf{c}(\mathbf{x}^{(i)})) \quad (10)$$

with $\mathbf{S}^{(i)}$ being the 3×3 correction matrix in our case (in general, the size of \mathbf{S} is equal to the number of the components in \mathbf{c} , \mathbf{f} , and \mathbf{s})

$$\mathbf{S}^{(i)} = \Delta \mathbf{F} \cdot \Delta \mathbf{C}^\dagger, \quad (11)$$

where

$$\Delta \mathbf{F} = [\mathbf{f}(\mathbf{x}^{(i)}) - \mathbf{f}(\mathbf{x}^{(i-1)}) \quad \cdots \quad \mathbf{f}(\mathbf{x}^{(i)}) - \mathbf{f}(\mathbf{x}^{(\max\{i-n, 0\})})], \quad (12)$$

and

$$\Delta \mathbf{C} = [\mathbf{c}(\mathbf{x}^{(i)}) - \mathbf{c}(\mathbf{x}^{(i-1)}) \quad \cdots \quad \mathbf{c}(\mathbf{x}^{(i)}) - \mathbf{c}(\mathbf{x}^{(\max\{i-n, 0\})})]. \quad (13)$$

The pseudoinverse, denoted by † , is defined as^{20,21}

$$\Delta \mathbf{C}^\dagger = \mathbf{V}_{\Delta \mathbf{C}} \boldsymbol{\Sigma}_{\Delta \mathbf{C}}^\dagger \mathbf{U}_{\Delta \mathbf{C}}^T, \quad (14)$$

where $\mathbf{U}_{\Delta \mathbf{C}}$, $\boldsymbol{\Sigma}_{\Delta \mathbf{C}}$, and $\mathbf{V}_{\Delta \mathbf{C}}$ are the factors in the singular value decomposition of the matrix $\Delta \mathbf{C}$. The matrix $\boldsymbol{\Sigma}_{\Delta \mathbf{C}}^\dagger$ is the result of inverting the nonzero entries in $\boldsymbol{\Sigma}_{\Delta \mathbf{C}}$, leaving the zeroes invariant. Upon convergence, the linear correction \mathbf{S}^* (being the limit of $\mathbf{S}^{(i)}$ with $i \rightarrow \infty$) maps the point $\mathbf{c}(\mathbf{x}^*)$ to $\mathbf{f}(\mathbf{x}^*)$, and the tangent plane for $\mathbf{c}(\mathbf{x})$ at $\mathbf{c}(\mathbf{x}^*)$ to the tangent plane for $\mathbf{f}(\mathbf{x})$ at $\mathbf{f}(\mathbf{x}^*)$. It should be noted that although MM does not explicitly use sensitivity information, the surrogate and the high-fidelity model Jacobians become more and more similar to each other towards the end of the MM optimization process (i.e., when $\|\mathbf{x}^{(i)} - \mathbf{x}^{(i-1)}\| \rightarrow 0$) so that the surrogate (approximately) satisfies both zero- and first-order consistency conditions with \mathbf{f} . This allows for a more precise identification of the high-fidelity model optimum. On the other hand, the correction matrix $\mathbf{S}^{(i)}$ can be defined using exact Jacobians of the low- and high-fidelity models if available.

The solution of algorithm (2) with the surrogate model (10) is carried out using the pattern search algorithm,^{24,25} and the termination conditions are the same as for the space mapping optimization algorithm (Sec. II.C.1). In the specific case of airfoils, where the model response vectors consist of three components (lift, drag, and cross-section area), the correction matrix \mathbf{S} should be identity with respect to the third components (the area is identical for both the low- and high-fidelity model).

III. Applications to Benchmark Problems

The direct and multi-fidelity optimization algorithms of Sec. II are applied to two benchmark aerodynamic design problems involving inviscid and viscous transonic flow past airfoil shapes. The optimization results are compared in terms of the design quality as well as the number of model evaluations and total optimization time.

A. Benchmark Case I: Drag Minimization of the NACA 0012 in Transonic Inviscid Flow

1. Problem Statement

The objective is to minimize the drag coefficient (C_d) of modified NACA 0012 airfoil section at a free-stream Mach number of $M_\infty = 0.85$ and an angle of attack $\alpha = 0$ deg. subject to a minimum thickness constraint. The optimization problem is stated as

$$\min_{\mathbf{l} \leq \mathbf{x} \leq \mathbf{u}} C_d, \quad (15)$$

where \mathbf{x} is the vector of design variables, and \mathbf{l} and \mathbf{u} are the lower and upper bounds, respectively. The thickness constraint is stated as

$$z(x) \geq z(x)_{\text{baseline}}, \quad (16)$$

where $z(x)$ is the airfoil thickness, $x \in [0,1]$ is the chord-wise location, and $z(x)_{\text{baseline}}$ is the thickness of the baseline airfoil, which is a modified version of the NACA 0012, defined as

$$z(x)_{\text{baseline}} = \pm 0.6 \left(0.2969\sqrt{x} - 0.1260x - 0.3516x^2 + 0.2843x^3 - 0.1036x^4 \right). \quad (17)$$

In our implementation, the objective function is set as $H(\mathbf{f}(\mathbf{x})) = C_d$ and the thickness constraint is handled directly. The design variables and their bounds are described as follows.

2. Design Variables

The airfoil shape design variables are defined by the parametrization method. The design variable vector is written as $\mathbf{x} = \mathbf{p}$, where \mathbf{p} is a vector of size $m \times 1$, with m being the total number of control parameters of the shape parameterization technique. In this work, we use B-spline curves (see, e.g., Farin²⁷) for the shape parametrization. The airfoil surfaces are written in parametric form as²⁷

$$x(t) = \sum_{i=1}^{n+1} X_i N_{i,k}(t), \quad z(t) = \sum_{i=1}^{n+1} Z_i N_{i,k}(t), \quad (18)$$

where (x,z) are the Cartesian coordinates of the surface, $N_{i,k}$ is the B-spline basis function of order k , (X_i, Z_i) are the coordinates of the B-spline control polygon, and $n+1$ is the total number of control points. Note that the surface description with (18) is continuous. The control points are used as design variables and allowed only to move freely vertically as shown in Fig. 2 (in this figure we only show the upper surface of the airfoil). Each designable control point is free to move in the vertical direction only. Thus, we have $\mathbf{x} = \mathbf{p} = [Z_1 \ Z_2 \ \dots \ Z_{n+1}]^T$ and the corresponding X_i are fixed during the optimization.

In Benchmark Case I, we use 10 control points, as shown in Fig. 2, where two are fixed at the leading- and trailing-edges, and the other ones can move in the vertical direction, yielding 8 design variables. Based on a fit to the modified NACA 0012 of (17), we set the x -locations of the free control points as $\mathbf{X} = [0 \ 0.0536 \ 0.2000 \ 0.4000 \ 0.5854 \ 0.7527 \ 0.8854 \ 0.9706]^T$. The initial design variable vector is $\mathbf{x} = [0.0185 \ 0.0474 \ 0.0654 \ 0.0633 \ 0.0486 \ 0.0323 \ 0.0161 \ 0.0043]^T$. The lower bound of \mathbf{x} is set as zero, i.e., $\mathbf{l} = \mathbf{0}$, and the upper bound is set as one, i.e., $\mathbf{u} = \mathbf{1}$.

3. Inviscid Aerodynamics Model

The Stanford University Unstructured (SU²) computer code²⁸ is utilized for the inviscid fluid flow simulations. The steady compressible Euler equations are solved with an implicit density-based formulation. The convective fluxes are calculated using the second order Jameson-Schmidt-Turkel (JST) scheme²⁹. Three multi-grid levels are used for solution acceleration. Asymptotic convergence to a steady state solution is obtained in each case. The flow

solver convergence criterion is the one that occurs first of the two: (i) the change in the drag coefficient value over the last 100 iterations is less than 10^{-4} , or (ii) a maximum number of iterations of 1,000 is met.

An O-type computational mesh is generated using Pointwise³⁰ (see Fig. 3). Since the airfoil is symmetrical and the angle of attack is fixed at zero, only the half-plane is considered. The farfield boundary is set 55 chord lengths away from the airfoil surface. The mesh density is controlled by the number of cells on the airfoil surface and the number of cells normal to the surface. The results of a grid convergence study, given in Table 1, revealed that a 512×512 mesh (shown number 5 in the table) is required for convergence within 0.1 drag count (1 drag count is $\Delta C_d = 10^{-4}$) when compared with the next mesh. Distance to the first grid point is $0.0015c$. The flow simulation for Mesh 5 takes about 4.2 minutes. An adjoint solution for the drag coefficient take approximately the same amount of time. It should be noted that throughout an optimization run the airfoil shape may change significantly and the flow and adjoint simulation times may vary depending on the particular shape.

For the optimization studies, Mesh 5 will be used as the high-fidelity model **f**, and Mesh 3 as the low-fidelity model **c** (used only for space mapping and manifold mapping). For the low-fidelity model, the maximum number of solver iterations is set to 300. Figure 4(a) shows the solver convergence of the low-fidelity model, and Fig. 4(b) gives a comparison of the low- and the high-fidelity models. The comparison indicates that the low-fidelity model may be a relatively good representation of the high-fidelity one.

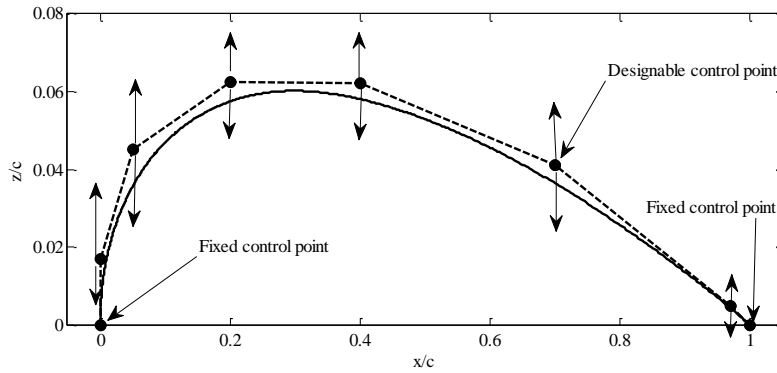


Figure 2. B-spline parameterization for the upper surface of the airfoil.

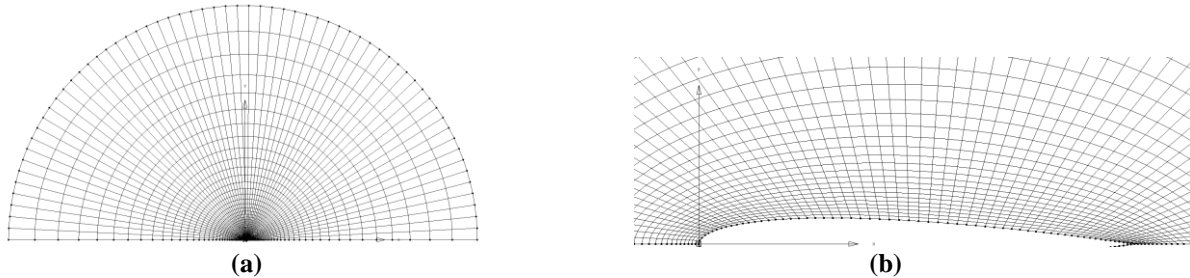


Figure 3. The half-plane O-mesh used in the inviscid model: (a) farfield view, (b) a view close to the surface.

Table 1. Grid convergence study for the baseline shape of BC I at $M = 0.85$ and $\alpha = 0.0^\circ$.

Mesh	Grid Size	C_l (cts)	C_d (cts)	Simulation Time* (min)
1	32×32 (961)	0.0	496.7194	0.29
2	64×64 (3,969)	0.0	480.7083	0.41
3	128×128 (16,129)	0.0	470.2201	0.71
4	256×256 (65,025)	0.0	469.3722	1.72
5	512×512 (261,121)	0.0	468.4470	4.24
6	$1,024 \times 1,024$ (1,046,529)	0.0	468.3714	24.60

* Computed on a high-performance cluster with 32 processors. Flow solution only.

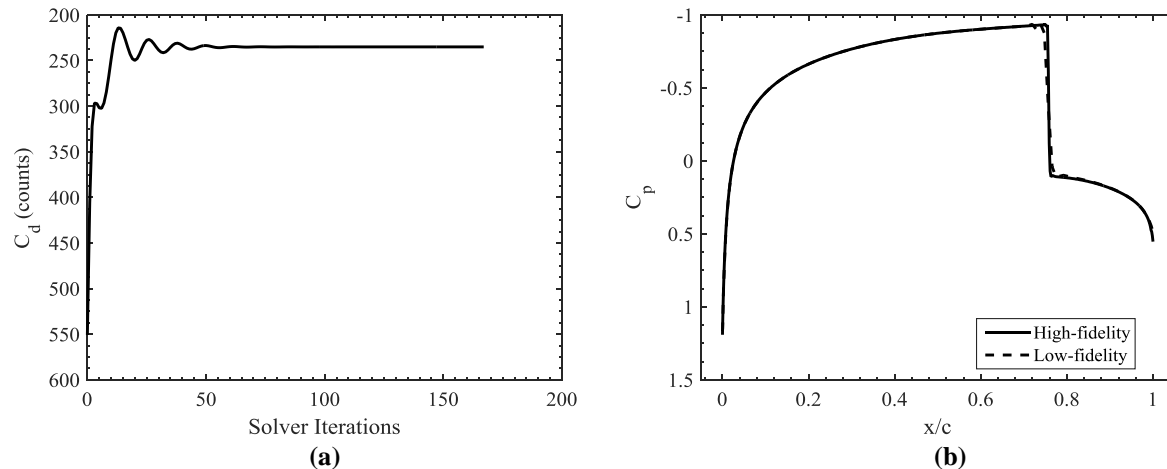


Figure 4. Inviscid flow simulation results for the modified NACA 0012 at $M = 0.85$ and $\alpha = 0.0^\circ$: (a) the evolution of the drag coefficient obtained by the low-fidelity model; (b) a comparison of the pressure distributions obtained by the high- and low-fidelity models.

4. Optimization Results

Benchmark Case I (BC I) is solved using the optimization algorithms listed in Table 2. Figure 5 shows the convergence history of the algorithms. In particular, Fig. 5(a) shows the convergence of the argument \mathbf{x} , and Fig. 5(b) shows the evolution of the objective function H (the drag coefficient in this case). The direct algorithms A and B terminate on the objective function, whereas the space mapping and manifold mapping algorithms terminate on the argument.

In terms of design quality, Direct B obtained the lowest drag coefficient value of 47.7 counts (Table 3). Direct A obtained a drag coefficient value of 55.1 counts, whereas the space mapping and manifold mapping algorithms converge to the same design with a drag coefficient value of 74.5 counts. Although, there is a significant difference in the drag coefficient values the overall shapes look very similar (see Fig. 6(a)). However, there is a slight difference between the shapes obtained by the direct algorithms and the multi-fidelity algorithms. In particular, the shapes obtained by the direct algorithms have a slightly fuller shape between $x/c = 0.6$ to $x/c = 0.8$ than the shapes obtained by the multi-fidelity algorithms. Other parts of the shapes are comparable. In terms of the pressure coefficient distributions, shown in Figs. 6(b), the shape obtained by Direct B has a distinctly lower peak near the leading-edge of the airfoil compared to the others. All the shapes have reduced the shock strength significantly when compared to the baseline pressure distribution. Figure 7 shows the pressure coefficient contours for all the shapes, including the baseline. A grid convergence study of the optimized shape obtained by manifold mapping indicates that the high-fidelity grid used in the optimization run (the 512×512 grid) is converged within 0.3 drag counts. This indicates that a finer mesh may have to be used for the high-fidelity model in order to ensure a drag coefficient resolution of less than 0.1 drag counts.

In terms of computational cost, the multi-fidelity algorithms need the least amount time. In particular, they need 4 high-fidelity model evaluations (N_f), and 778 low-fidelity model evaluations (N_c); which, in total, is equivalent to less than 150 high-fidelity model evaluations (N_{tot}). The total optimization time is about 459 minutes. Direct B needed 391 high-fidelity model evaluations (includes both flow and adjoint solutions) and the total optimization time was about 4,949 minutes. Note that the multi-fidelity methods used in this study only require the flow solutions but not the adjoint solutions like the gradient-based algorithm. Consequently, the space mapping and manifold mapping algorithms are more efficient than the Direct B algorithm. Direct A needed 1,383 high-fidelity model evaluations (only flow solutions) and the total optimization time was about 6,939 minutes.

Table 2. Details of the optimization algorithms used for BC I.

Algorithm	Driver	Model	Mesh for \mathbf{f}	Mesh for \mathbf{c}	Adjoints	Trust Region
Direct A	Pattern search	\mathbf{f}	5	N/A	N/A	N/A
Direct B	MATLAB's fmincon	(3)	5	N/A	Yes	Yes
Space Mapping	Pattern search	(4)	5	3	No	Yes
Manifold Mapping	Pattern search	(10)	5	3	No	Yes

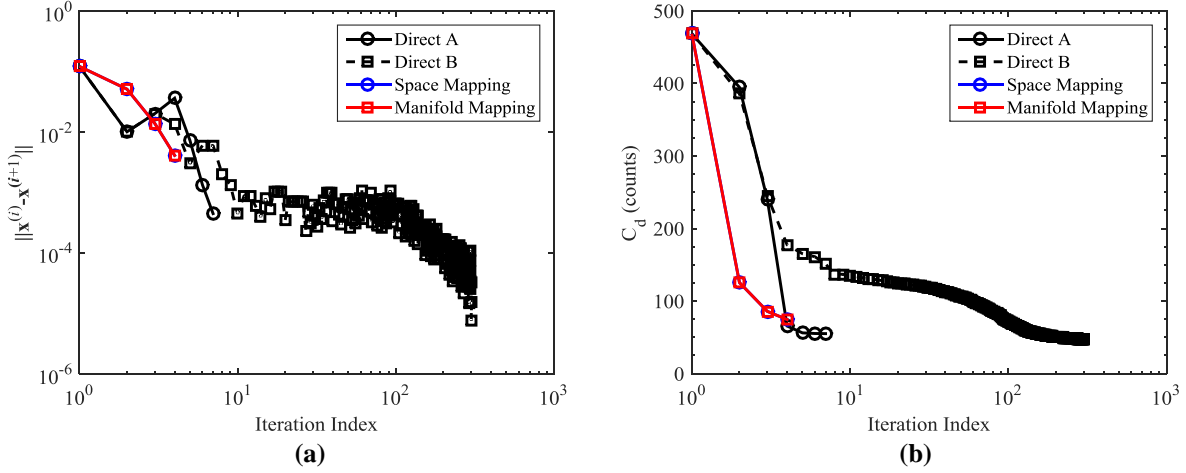


Figure 5. BC I convergence histories of the optimization runs.

Table 3. Optimization results for BC I.

Parameter/Method	Baseline	Direct A	Direct B	SM	MM
C_l (l.c.)	0.0	0.0	0.0	0.0	0.0
C_d (d.c.)	468.45	55.10	47.68	74.53	74.53
N_c	—	—	—	778	778
N_f	—	1,383	391*	4	4
N_{tot}	—	1,383	391*	< 150	< 150
t_c (min)	—	—	—	447.0	445.8
t_f (min)	—	6,939	4,494	12.3	13.1
t_{tot} (min)	—	6,939	4,494	459.3	458.9

* Primary flow solutions as well as adjoint solutions.

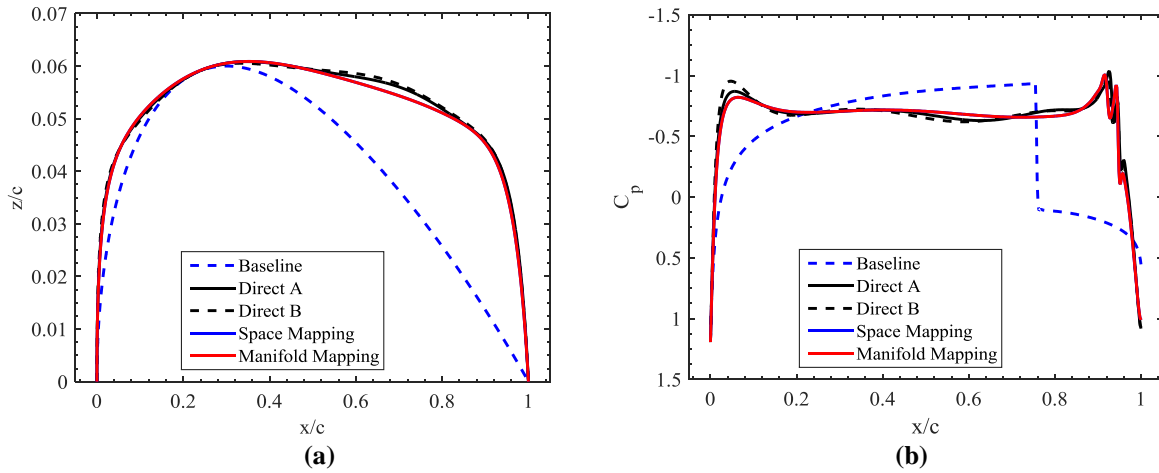
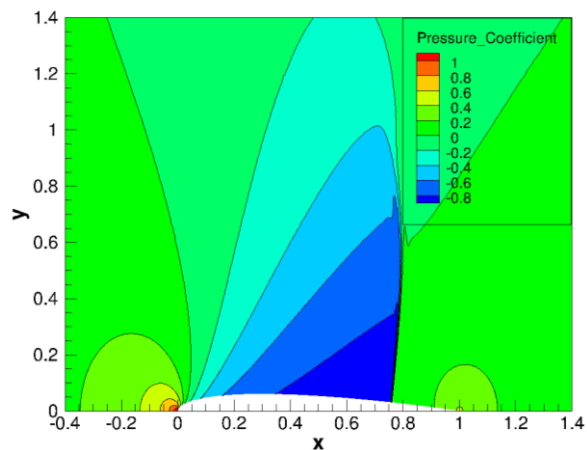


Figure 6. BC I baseline and optimized characteristics: (a) shapes, (b) pressure coefficient distributions.

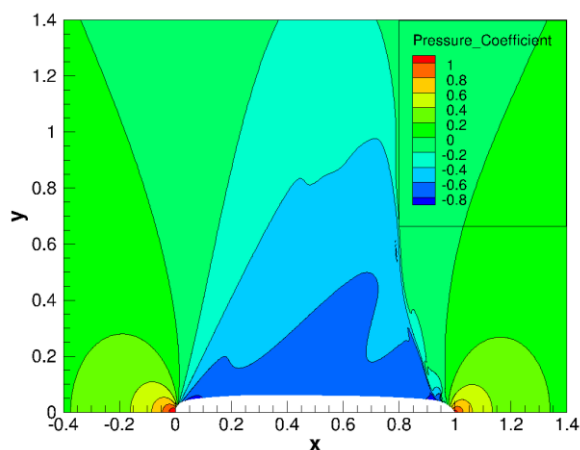
Table 4. Grid convergence study for the optimized MM shape of BC I at $M = 0.85$ and $\alpha = 0.0^\circ$.

Mesh	Grid Size	C_l (cts)	C_d (cts)	Simulation Time* (min)
1	32×32 (961)	0.0	272.7192	0.25
2	64×64 (3,969)	0.0	129.5981	0.42
3	128×128 (16,129)	0.0	83.0096	0.76
4	256×256 (65,025)	0.0	77.2443	1.59
5	512×512 (261,121)	0.0	74.5209	4.41
6	$1,024 \times 1,024$ (1,046,529)	0.0	74.1940	23.34

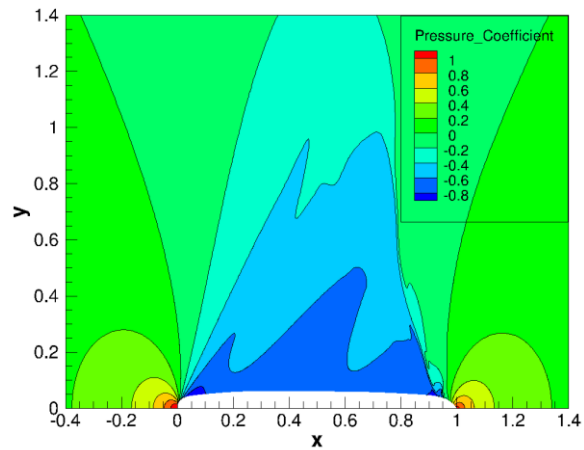
* Computed on a high-performance cluster with 32 processors. Flow solution only.



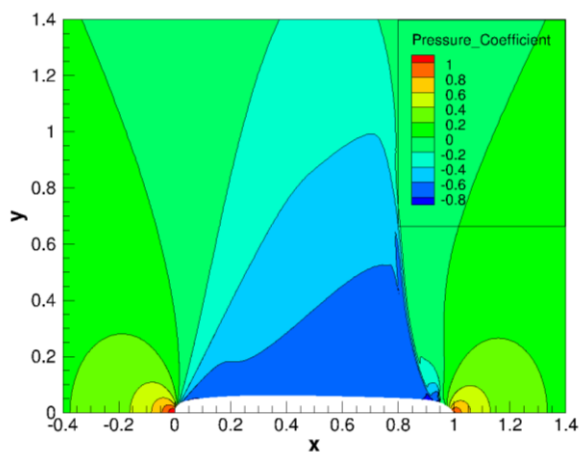
(a) Baseline



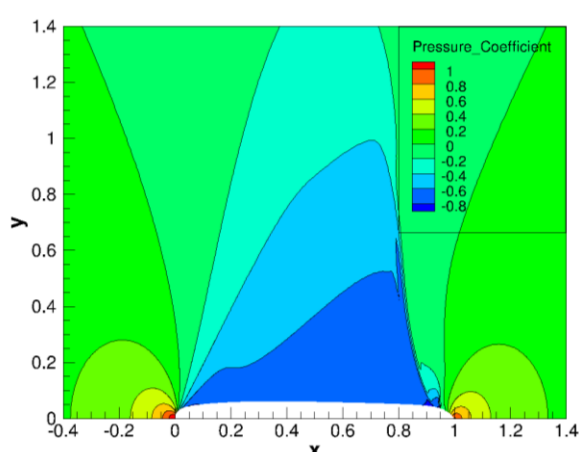
(c) Direct A



(d) Direct B



(e) Space Mapping



(f) Manifold Mapping

Figure 7. BC I pressure coefficient contours for baseline and optimized shapes.

B. Benchmark Case II: Constrained Drag Minimization of the RAE 2822 in Transonic Viscous Flow

1. Problem Statement

The objective is to minimize the drag coefficient (C_d) of the RAE 2822 at a free-stream Mach number of $M_\infty = 0.734$, lift coefficient of 0.824, and Reynolds number of 6.5×10^6 subject to an area and pitching moment constraint. The task is to solve the following constrained optimization problem:

Solve

$$\min_{\mathbf{l} \leq \mathbf{x} \leq \mathbf{u}} C_d, \quad (19)$$

subject to the following constraints

$$C_l = 0.824, \quad (20)$$

$$C_m \geq -0.092, \quad (21)$$

$$A \geq A_{\text{baseline}}, \quad (22)$$

where C_m is the moment coefficient and A is the airfoil cross-sectional area nondimensionalized with the chord length squared.

The constant lift coefficient constraint (20) is implicitly satisfied in the flow solver by using the angle of attack as a dummy parameter (see Sec. III.B.3). In the implementation of the multi-fidelity algorithms, the pitching moment and cross-sectional area constraints (21) and (22), respectively, are handled through a penalty function. In the direct optimization algorithms, those constraints are handled directly.

2. Design Variables

The B-spline parameterization approach, described in Sec. III.A.2, is used in Benchmark Case II for the upper and lower surfaces. We use 10 control points, as shown in Fig. 2, where two are fixed at the leading- and trailing-edges, and the other ones, 4 for each surface, can move in the vertical direction. This yields 8 design variables. Based on a fit to the RAE 2822, we set the x -locations of the free control points as: $\mathbf{X} = [\mathbf{X}_u; \mathbf{X}_l]^T = [0.0 \ 0.15 \ 0.45 \ 0.80; 0.0 \ 0.35 \ 0.60 \ 0.90]^T$. The initial design variable vector is $\mathbf{x} = [\mathbf{x}_u; \mathbf{x}_l]^T = [0.0175 \ 0.0498 \ 0.0688 \ 0.0406; -0.0291 \ -0.0679 \ -0.0384 \ 0.0054]^T$. The lower bound of \mathbf{x} is set as $\mathbf{l} = [0 \ 0 \ 0 \ 0; -1 \ -1 \ -1 \ -1]^T$, and the upper bound is set as $\mathbf{u} = [1 \ 1 \ 1 \ 1; 0 \ 0 \ 0 \ 0]^T$.

3. Viscous Aerodynamics Model

The SU² implicit density-based flow solver²⁸ is used for the viscous case, solving the steady compressible Reynolds-averaged Navier-Stokes (RANS) equations with the Spalart-Allmaras turbulent model³¹. The convective flux will be calculated using the second order JST scheme²⁹. One multi-grid level is used for solution acceleration. The turbulent variables are convected using a first-order scalar upwind method. The flow solver convergence criterion is the one that occurs first of the two: (i) the change in the drag coefficient value over the last 100 iterations is less than 10^{-5} , or (ii) a maximum number of iterations of 5,000 is met.

The grids are generated using the hyperbolic C-mesh of Kinsey and Barth³² (see Fig. 8). The farfield is set 100 chords away from the airfoil surface. The grid points are clustered at the trailing edge and the leading edge of the airfoil to give a minimum streamwise spacing of $0.001c$, and the distance from the airfoil surface to the first node is $10^{-5}c$. The grid density is controlled by the number of points in the streamwise direction (N_s), and the number of points in the direction normal to airfoil surface (N_n). We set the number of points in the wake region equal to the number in the normal direction. The grid sizes are denoted by $N_s \times N_n$. Table 5 gives the results of a grid convergence study using the RAE 2822 airfoil at $M = 0.734$ and $C_l = 0.824$. The constant lift condition is determined by externally changing the angle of attack using a numerical optimization algorithm. Typically, 3 to 4 simulations are needed. The simulation times presented in Table 5 give the overall time to compute the constant lift condition. The times do not include the time it takes to calculate the adjoint solutions.

For the optimization studies, we use Mesh 2 for the high-fidelity model **f** and Mesh 1 for the low-fidelity model **c**. The low-fidelity model convergence criteria is the same as the high-fidelity one, but with the following values: drag coefficient convergence set to 10^{-4} , and the maximum number of iterations is set to 2,000. Fig. 9(a) shows that the low-fidelity solver is converged well within the 2,000 iteration limit, and Fig. 9(b) shows that the low-fidelity model is a good representation of high-fidelity one in terms of the pressure coefficient distributions.

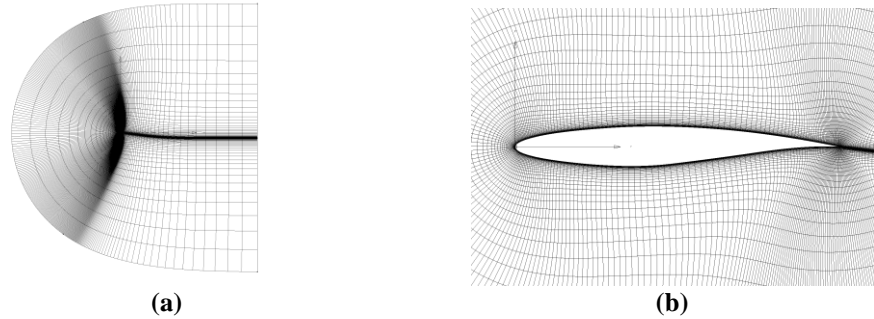


Figure 8. The hyperbolic C-mesh used in the viscous model: (a) farfield view, (b) view close to the surface.

Table 5. Grid convergence study for the baseline shape of Benchmark Case II.

Mesh	Grid Size	C_l (cts)	C_d (cts)	Simulation Time* (min)
1	120×40 (8,196)	82.39	257.59	5.5
2	240×80 (32,396)	82.35	220.28	19.0
3	480×160 (128,796)	82.40	204.67	77.2
4	960×320 (513,596)	82.36	198.65	518.8
5	$1,920 \times 640$ (2,051,196)	82.41	203.93	2,269.8

* Computed on a high-performance cluster with 32 processors. Flow solution only.

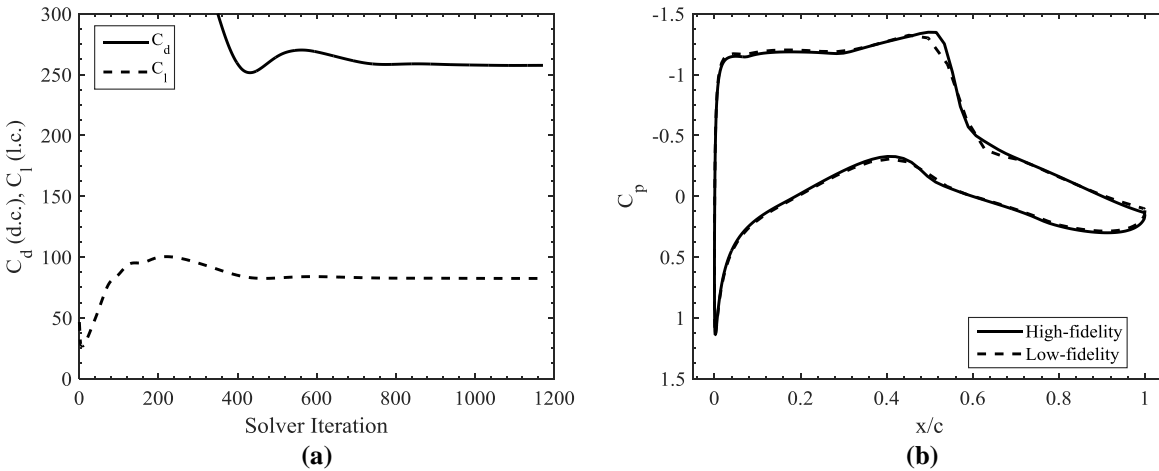


Figure 9. Viscous flow simulation results for RAE 2822 at $M = 0.734$ and $C_l = 0.824$: (a) the evolution of the lift and drag coefficients obtained by the low-fidelity model; (b) a comparison of the pressure distributions obtained by the high- and low-fidelity models.

4. Optimization Results

Benchmark Case II (BC II) is solved using Direct B, space mapping (SM), and manifold mapping (MM) algorithms as described in Table 2, but using Meshes 2 and 1 of Table 5 for the high- and low-fidelity models, respectively. Figure 10 shows the convergence history of the algorithms. The Direct B algorithm was unsuccessful, most likely due to excessive numerical noise of the chosen high-fidelity model, and changes the design only slightly; terminating after 4 design iterations based on the objective function. The multi-fidelity algorithms are, however, able to make significant reduction in the objective function and terminate after 3 design iterations based on the argument.

As can be seen by Table 6, the SM algorithm reduces the drag coefficient value from 220.3 counts to 131.4 counts (or by 88.9 counts), whereas the MM reduces it to 142 counts (or by 78.3 counts). Direct B reduced the drag coefficient value to 218.6 counts (or by 1.7 counts). Figure 11 shows the optimized shapes and pressure coefficient distributions. Figure 12 shows the pressure coefficient contours. Clearly, the SM and MM reduce the shock strength significantly. However, the lift coefficient and cross-sectional area constraints are slightly violated for both SM and

MM. In particular, the lift coefficients are less than 0.04 counts below the constraint value of 82.4 counts, and the cross-sectional areas are 1.5% below the baseline value of 0.0779. These violations are minor. The Direct B algorithm violates the pitching moment coefficient constraint is slightly (or by less than 1%).

The optimization cost of the SM and MM algorithms is comparable. SM needs less than 131 equivalent high-fidelity model evaluations (14 high-fidelity and 263 low-fidelity), and MM needs less than 125 high-fidelity equivalent calls (14 high-fidelity and 210 low-fidelity). In terms of time, SM took 17.8 hours and MM 17.4 hours.

Tables 5 and 7 indicate that the meshes used in the studies here are not converged. Future studies will use Mesh 5 (around 2 million cells) as the high-fidelity model to ensure converged flow solutions.

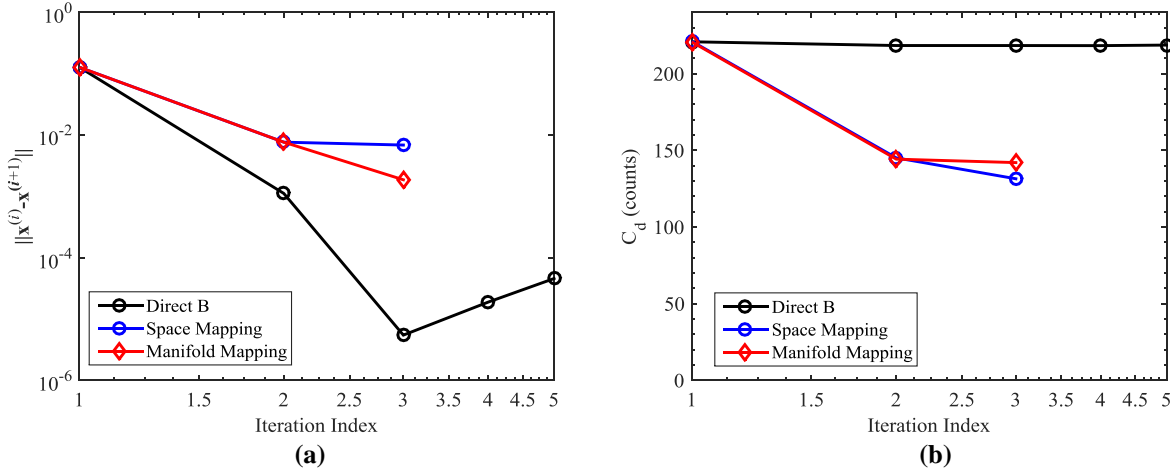


Figure 10. BC II convergence histories of the optimization runs.

Table 6. Optimization results for BC II.

Parameter/Method	Baseline	Direct B	SM	MM
C_l (l.c.)	82.35	82.41	82.39	82.36
C_d (d.c.)	220.28	218.60	131.41	141.96
$C_{m,c/4}$	-0.0905	-0.0925	-0.0917	-0.0904
A	0.0779	0.0782	0.0767	0.0767
N_c	—	—	263	210
N_f	—	54*	14	14
N_{tot}	—	54*	< 131	< 125
t_c (min)	—	—	952.9	924.6
t_f (min)	—	237.2	114.6	116.7
t_{tot} (min)	—	237.2	1,067.5	1,041.3

* Primary flow solutions as well as adjoint solutions.

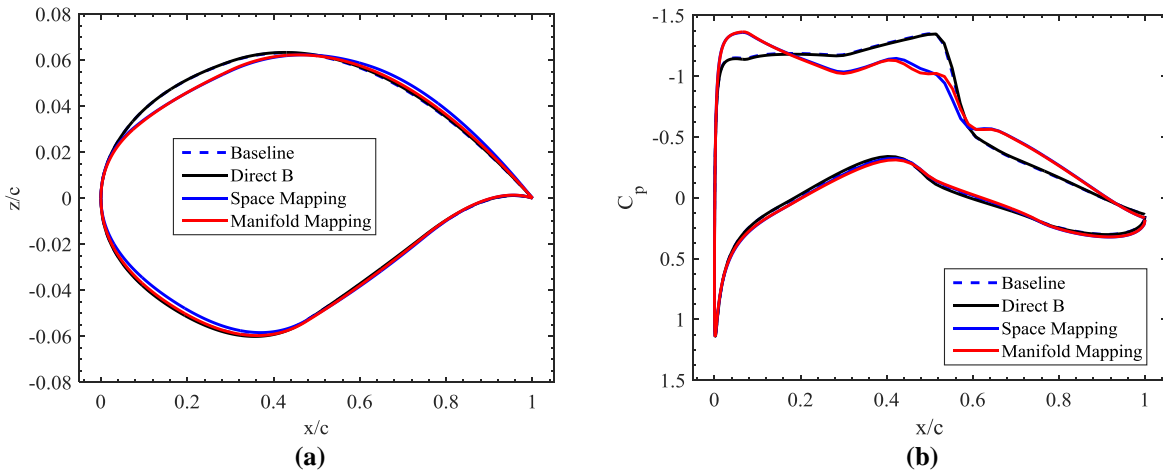
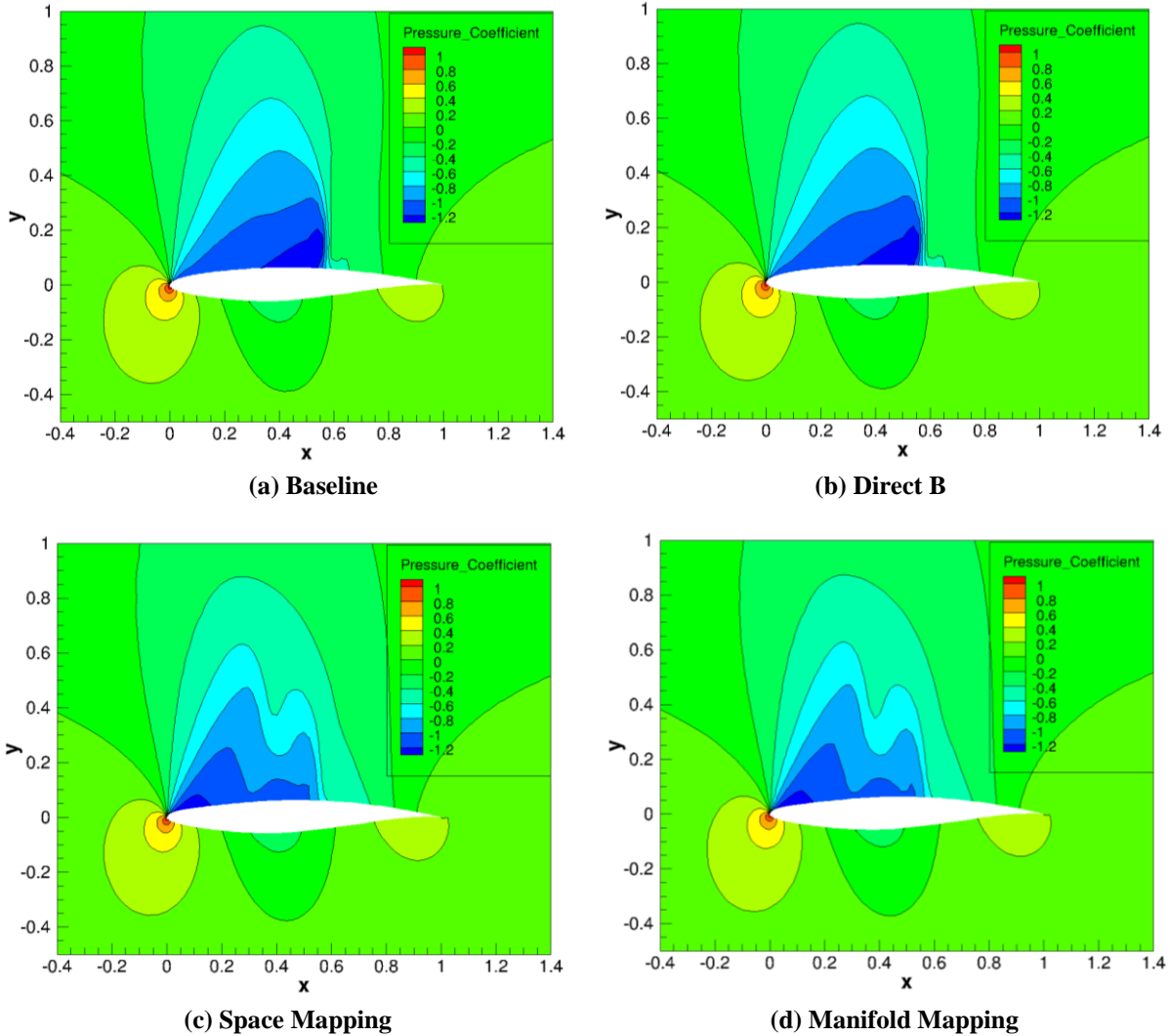


Figure 11. BC II baseline and optimized characteristics: (a) shapes, (b) pressure coefficient distributions.

Table 7. Grid convergence study for the MM optimized shape of BC II.

Mesh	Grid Size	C_l (cts)	C_d (cts)	Simulation Time* (min)
1	120 × 40 (8,196)	0.8239	184.08	6.8
2	240 × 80 (32,396)	0.8236	141.78	21.2
3	480 × 160 (128,796)	0.8235	133.85	55.1
4	960 × 320 (513,596)	0.8236	130.57	532.3
5	1,920 × 640 (2,051,196)	0.8239	134.48	2,880.1

* Computed on a high-performance cluster with 32 processors. Flow solution only.

**Figure 12. BC II pressure coefficient contours for baseline and optimized shapes.**

IV. Conclusion

A robust and computationally efficient optimization methodology for aerodynamic design is presented. The approach uses low-fidelity models corrected by the manifold mapping technique to create fast and reliable surrogate which is utilized to search for approximate optimum designs of an expensive high-fidelity model at a low CPU cost. The manifold mapping correction is applied both to the objectives and constraints that ensures a good alignment between the surrogate and the high-fidelity model. The proposed approach is applied to benchmark cases involving lift-constrained airfoil drag minimization in two-dimensional inviscid and viscous transonic flows. The results of these benchmark cases show that the optimized designs are obtained at a significantly lower computational cost

compared to the direct high-fidelity model optimization with adjoint sensitivity information when using 8 design variables. The cost is comparable with the space mapping algorithm which is also based on multi-fidelity models.

The version of the manifold mapping approach utilized in this paper, as well as the space mapping one, do not require gradient information. Since our implementation uses pattern search to optimize the surrogate model, the cost of increasing the number of design variables will grow quickly. Future work will, therefore, investigate alternatives to efficiently optimize the surrogate model. In particular, we will investigate the extension of manifold mapping using adjoint sensitivity information, as well as adding techniques for the reduction of the design space dimensionality.

Another possible future investigation is to combine space mapping and manifold mapping with space mapping used as a preconditioner for the low-fidelity model. In such a case, the multi-point space mapping surrogate may be established using, e.g., star-distribution design of experiments in order to improve the global matching between the models (in which case only the global parameters **A** and **D** need to be calculated), and the MM correction may be applied on the top of SM.

Finally, in the cases considered here, the objective functions are all scalars. In such cases, the manifold mapping algorithm yields comparable results as the space mapping algorithm, as demonstrated through the benchmark cases. Manifold mapping typically works well for design cases with vector-valued responses. Therefore, manifold mapping may work well for inverse design cases, such as when a target pressure coefficient distribution is prescribed and the task is to find the airfoil or wing shapes yielding the prescribed target. Another example of a vector-valued response is multi-point design where an aerodynamic surface is optimized at several operating conditions, e.g., for several pairs of Mach numbers and lift coefficients. This will be the subject of future work.

References

- ¹Leoviriyakit, K., Kim, S., and Jameson, A., "Viscous Aerodynamic Shape Optimization of Wings including Planform Variables," *21st Applied Aerodynamics Conference*, Orlando, Florida, June 23-26, 2003.
- ²Braembussche, R.A., "Numerical Optimization for Advanced Turbomachinery Design," In *Optimization and Computational Fluid Dynamics*, Thevenin, D. and Janiga, G., editors, Springer, 2008, pp. 147-189.
- ³Mader, C.A., and Martins, J.R.R.A., "Derivatives for Time-Spectral Computational Fluid Dynamics Using an Automatic Differentiation Adjoint," *AIAA Journal*, Vol. 50, No. 12 (2012), pp. 2809-2819. doi: 10.2514/1.J051658
- ⁴Mousavi, A., and Nadarajah, S., "Heat Transfer Optimization of Gas Turbine Blades Using an Adjoint Approach," *13th AIAA/ISSMO Multidisciplinary Analysis Optimization Conference*, AIAA Paper 2010-9048, Fort Worth, Texas, Sept. 13-15, 2010.
- ⁵Leung, T.M., and Zingg, D.W., "Aerodynamic Shape Optimization of Wings Using a Parallel Newton-Krylov Approach," *AIAA Journal*, Vol. 50, No. 3 (2012), pp. 540-550.
- ⁶Epstein, B., and Peigin, S., "Constrained Aerodynamic Optimization of Three-Dimensional Wings Driven by Navier-Stokes Computations," *AIAA Journal*, Vol. 43, No. 9 (2005), pp. 1946-1957.
- ⁷Nocedal, J., Wright, S.J., *Numerical Optimization*, Springer, 2006.
- ⁸Kim, S., Hosseini, K., Leoviriyakit, K., and Jameson, A., "Enhancement of Class of Adjoint Design Methods via Optimization of Parameters," *AIAA Journal*, Vol. 48, No. 6 (2010), pp. 1072-1076.
- ⁹Schmidt, S., Gauger, N., Ilic, C., Schulz, V., "Three Dimensional Large Scale Aerodynamic Shape Optimization based on Shape Calculus," *41st AIAA Fluid Dynamics Conference and Exhibit*, AIAA Paper 2011-3718, Honolulu, Hawaii, June 27-30, 2011.
- ¹⁰Queipo, N.V., Haftka, R.T., Shyy, W., Goel, T., Vaidyanathan, R., and Tucker, P.K., "Surrogate-Based Analysis and Optimization," *Progress in Aerospace Sciences*, Vol. 41, No. 1, 2005, pp. 1-28.
- ¹¹Forrester, A.I.J., and Keane, A.J., "Recent advances in surrogate-based optimization," *Progress in Aerospace Sciences*, Vol. 45, No. 1-3, 2009, pp. 50-79.
- ¹²Koziel, S., Echeverría-Ciaurri, D., and Leifsson, L., "Surrogate-based methods," in S. Koziel and X.S. Yang (Eds.) *Computational Optimization, Methods and Algorithms*, Series: Studies in Computational Intelligence, Springer-Verlag, pp. 33-60, 2011.
- ¹³Alexandrov, N.M., Lewis, R.M., Gumbert, C.R., Green, L.L., and Newman, P.A., "Optimization with Variable-Fidelity Models Applied to Wing Design," *38th Aerospace Sciences Meeting & Exhibit*, Reno, NV, AIAA Paper 2000-0841, Jan. 2000.
- ¹⁴Robinson, T.D., Eldred, M.S., Willcox, K.E., and Haimes, R., "Surrogate-Based Optimization Using Multifidelity Models with Variable Parameterization and Corrected Space Mapping," *AIAA Journal*, vol. 46, no. 11, 2008.
- ¹⁵Koziel, S., Cheng, Q.S., and Bandler, J.W., "Space mapping," *IEEE Microwave Magazine*, vol. 9, no. 6, pp. 105-122, Dec. 2008.
- ¹⁶Koziel, S., and Leifsson, L., "Knowledge-based airfoil shape optimization using space mapping," AIAA Paper 2012-3016, *30th AIAA Applied Aerodynamics Conference*, New Orleans, Louisiana, June 25-28, 2012.
- ¹⁷Koziel, S., and Leifsson, L., "Adaptive Response Correction for Surrogate-Based Airfoil Shape Optimization," *30th AIAA Applied Aerodynamics Conference*, New Orleans, Louisiana, June 25-28, 2012.
- ¹⁸Koziel, S., and Leifsson, L., "Multi-Fidelity Airfoil Optimization with Adaptive Response Prediction," *14th AIAA/ISSMO*

Multidisciplinary Analysis and Optimization Conference, Sept. 17-19, Indianapolis, Indiana, 2012.

¹⁹ Koziel, S., and Leifsson, L., "Surrogate-Based Aerodynamic Shape Optimization by Variable-Resolution Models," *AIAA Journal*, vol. 51, no. 1, 2013, pp. 94-106.

²⁰ Echeverría-Ciaurri, D., and Hemker, P.W., "Manifold Mapping: a Two-Level Optimization Technique," *Computing and Visualization in Science*, 11, pp. 193-206, 2008.

²¹ Koziel, S., and Echeverría-Ciaurri, D., "Reliable Simulation-Driven Design Optimization of Microwave Structures Using Manifold Mapping," *Progress in Electromagnetic Research B (PIER B)*, 26, pp. 361-382, 2010.

²² Jameson, A., "Aerodynamic Design via Control Theory," *Journal of Scientific Computing*, Vol. 3, 1988, pp. 233-260.

²³ Conn, A.R., Gould, N.I.M., and Toint, P.L., *Trust Region Methods*, MPS-SIAM Series on Optimization, 2000.

²⁴ Leifsson, L. and Koziel, S., *Simulation-Driven Aerodynamic Design Using Variable-Fidelity Models*, Imperial College Press, London, UK, 2015.

²⁵ Koziel, S., "Multi-fidelity multi-grid design optimization of planar microwave structures with Sonnet," *International Review of Progress in Applied Computational Electromagnetics*, Tampere, Finland, 2010, pp. 719-724.

²⁶ MATLAB V15.0, Mathworks Inc., Corporate Headquarters, 3 Apple Hill Drive, Natick, MA 01760-2098, USA.

²⁷ Farin G., *Curves and Surfaces for Computer Aided Geometric Design*, Boston, MA: Academic Press, 1993.

²⁸ Palacios, F., Colonna, M. R., Aranake, A. C., Campos, A., Copeland, S. R., Economon, T. D., Lonkar, A. K., Lukaczyk, T. W., Taylor, T. W. R., and Alonso, J. J., "Stanford University Unstructured (SU²): An open-source integrated computational environment for multi-physics simulation and design," AIAA Paper 2013-0287, 51st AIAA Aerospace Sciences Meeting and Exhibit, Grapevine, Texas, USA, 2013.

²⁹ Jameson, A., Schmidt, W., and Turkel, E., "Numerical Solution of the Euler Equations by Finite Volume Methods Using Runge-Kutta Time-Stepping Schemes," AIAA 1981-1259, AIAA 14th Fluid and Plasma Dynamic Conference, Palo Alto, CA, June 23-25, 1981.

³⁰ Pointwise V17.3R2, Pointwise Inc., 213 South Jennings Avenue, Fort Worth, Texas, 76104-1107, USA.

³¹ Spalart, P. R. and Allmaras, S. R., "A One Equation Turbulence Model for Aerodynamic Flows", AIAA-Paper-92-0439, 38th AIAA Aerospace Sciences Meeting and Exhibit, Reno, NV, January 6-9, 1992.

³² Kinsey, D. W., and Barth, T. J., "Description of a Hyperbolic Grid Generation Procedure for Arbitrary Two-Dimensional Bodies," AFWAL TM 84-191-FIMM, 1984.